Durham Research Online

Additional information:

Discrete Curvature Representations for Noise Robust Image Corner Detection

Weichuan Zhang, Changming Sun, Toby Breckon, Naif Alshammari

Abstract—Image corner detection is very important in the fields of image analysis and computer vision. Curvature calculation techniques are used in many contour-based corner detectors. We identify that existing calculation of curvature is sensitive to local variation and noise in the discrete domain and does not perform well when corners are closely located. In this paper, discrete curvature representations of single and double corner models are investigated and obtained. A number of model properties have been discovered which help us detect corners on contours. It is shown that the proposed method has a high corner resolution (the ability to accurately detect neighbouring corners) and a corresponding corner resolution constant is also derived. Meanwhile, this method is less sensitive to any local variations and noise on the contour; and false corner detection is less likely to occur. The proposed detector is compared with seven state-of-the-art detectors. Three test images with ground truths are used to assess the detection capability and localization accuracy of these methods in noise-free and cases with different noise levels. Twenty-four images with various scenes without ground truths are used to evaluate their repeatability under affine transformation, JPEG compression, and noise degradations. The experimental results show that our proposed detector attains a better overall performance.

Index Terms—Discrete curvature representations, corner detection, corner resolution, noise robustness.

I. Introduction

IMAGE corner detection is an extremely important task in image analysis and computer vision. Applications include motion tracking, object recognition, and stereo matching [1], [2]. A corner can be defined as a point with low self-similarity or a location where variations of the image intensity in all directions are significant [3]. Alternatively, a corner may be defined as a location on an edge contour where the contour changes direction sharply or where a point has a high curvature [4].

A. Related works

In general, most existing corner detection algorithms can be divided into three categories [5]: intensity-based methods [3], [6]–[16], model-based methods [5], [17]–[25], and contour-based methods [4], [26]–[42].

W. Zhang is with College of Electrical and Information, Xi'an Polytechnic University, Xi'an, 710048, China, and with CSIRO Data61, PO Box 76, Epping, NSW 1710, Australia.
E-mail: zwc2003@163.com, weichuan.zhang@csiro.au
C. Sun is with CSIRO Data61, PO Box 76, Epping, NSW 1710, Australia.
E-mail: changming.sun@csiro.au
T. Breckon is with Durham University, UK.
E-mail: toby.breckon@durham.ac.uk
N. Alshammari is with Durham University, UK.
E-mail: naif.alshammari@durham.ac.uk

Intensity-based methods extract corners directly from the input images by measuring image pixel values. One of the earliest methods [3] considers corners as points which have low self-similarity in all directions. The self-similarity of a point can be measured by using the sum of squared differences (SSD) between their associated image patches. This is the basis for a large number of corner detectors. Harris and Stephens [6] proposed to approximate the SSD by the local autocorrelation matrix. The corner measure is constructed from the two eigenvalues of the matrix. The Harris detector was shown to be optimal only for L-junctions [7]. More recently, the Harris detector was extended with searches over scale and space in [8]–[16], which detect corners by identifying the characteristic scale of a corner.

Model-based methods find corners by fitting a small patch of image with predefined models. Deriche and Giraudon [17] analyzed the characterization of wedge and Y-type corners by using the Gaussian filter. In [18] and its variants [22], corners are defined as the smallest univalue segment assimilating nucleus points. In [19], [20], junctions are defined as points in an image where two or more piecewise constant wedges meet at the central point. Shui and Zhang [5] applied the anisotropic Gaussian directional derivative filters [43] to derive the representations of L-type, Y-type, X-type, and star-type corners and detect corners. Xia et al. [24] introduced a junction detection method based on the contrario detection theory [44], called a contrario junction detection. Pham et al. [25] presented a junction detection method where junctions are computed by searching for optimal meeting points of median lines in line-drawing images.

Contour-based methods first extract digital curves from the input image using some edge detectors and then analyse the contour shapes to detect corners. The curvature scale space (CSS) [26] is widely used in the contour-based methods [28]–[33]. The authors in these methods first smooth the curves with single- or multi-scale Gaussian filters. Subsequently, they compute the curvature at each point of the smoothed curves. The absolute maximal curvature points at single- or multi-scales are combined for corner detection. It is indicated [34]–[38] that the existing CSS corner detectors suffer from two main problems. On the one hand, the CSS curvature estimation technique is sensitive to local variation and noise on the curve. On the other hand, it is a difficult task to select an appropriate Gaussian scale to smooth the curve. To alleviate the aforementioned problems, many novel techniques, including multi-scale curvature product (MSCP) [29], direct curvature scale space [30], adaptive local threshold based on region of support [31], chord-to-point distance accumulation

(CPDA) [34], affine-length parametrizations instead of the arc-length [35], gradient correlation matrices (GCM) of planar curves [36], multi-direction Gabor filters [37], angle difference of principal directions [38], triangular theory [39], Laplacian scale-space [40], and corner detection [42] based on approximation discrete curvature calculation (ADCC) [45] are proposed to extract corners from the edge contours.

B. Contributions and outline

In this work, our interest lies in the contour-based corner detection algorithms. The existing contour-based methods [26], [28], [29], [31], [33], [41] usually first extract planar curves from the input image using some edge detectors and then search for local curvature maximal points along those curves. The afore-mentioned methods detect corners based on existing discrete curvature techniques. Our research shows that the existing discrete curvature techniques suffer from two main problems: (1) Errors in curvature calculation; (2) Sensitive to local variation and noise. Inspired by the multi-scale theory [46] that an object contains local features at many different scales, three typical corner models [26] (the END, STAIR, and L models) are used to construct the scale space map [26], [28], [30], [33], [40], [41] and to analyse the tracks of extreme points in scale space. The scale space map consists of the extreme points of curvature at a full range of smoothing scales [37], [36], [47] or at many significant scales [28], [33]. Multi-scale methods were mentioned to suffer from at least two defects [5], [31], [34], [37], [38]. The multi-scale curvature estimation technique is sensitive to local variations and noises on the contour. It is a difficult task to select appropriate Gaussian scales to smooth the contour. Large-scale Gaussian filters suppress noise well but degrade corner localization while small-scale filters preserve high precision in localization but are highly noise sensitive. Meanwhile, there are no existing work which deals explicitly with corner resolution which represents the ability to exactly detect adjacent corners. Corner resolution has a great effect on the detection and localization for neighbouring corners. Furthermore, our investigation revealed that in the existing contour-based corner detectors the corner detection accuracy, corner resolution, and noise robustness issues have not been considered simultaneously.

In this paper, discrete curvature representations of the three typical corner models [26] are derived. The properties of the representations are investigated and specified, and these properties enable us to propose a new corner detection algorithm. It is shown that the proposed method is robust to local variation and noise on the contour, and the method also has a high corner resolution. A corner resolution constant is also derived. This approach is less sensitive to the local variation and noise on the contour while maintaining the capabilities of high corner resolution, detection capability, localization accuracy, and real-time processing. This is impossible for the existing contour-based corner detectors [26], [28], [30], [33], [40], [41].

In this paper, the proposed corner detector is compared with seven state-of-the-art corner detectors (MSCP [29], He & Yung [31], CPDA [34], ARCSS [35], GCM [36], ANDD [5], and ADCC [42]) by using two commonly used test images with ground truths to evaluate the detection capability and localization accuracy for cases with noise-free and different noise levels. Twenty-four images with different scenes without ground truths are used to assess the repeatability under affine transformations, JPEG compression, and noise degradation of images. The experimental results show that the proposed method attains a better overall performance.

The following is the organization of the remainder of this paper. In Section 2, the existing curvature computation techniques and its weaknesses are discussed, and a new discrete curvature calculation is proposed. Discrete curvature representations of three typical corner models are derived. Section 3 details the properties of the discrete curvature representations. In Section 4, a new corner measure and a novel detection algorithm are presented. Section 5 presents and discusses the experimental results. Finally, our conclusions are presented in Section 6.

II. DISCRETE CURVATURE REPRESENTATIONS OF CORNERS

In this section, we first introduce the existing discrete curvature technique. Subsequently, the weakness of the technique is identified and analysed. Thirdly, a novel discrete curvature calculation is formulated and discrete curvature representations of corners on edge contour are presented.

A. The problem of discrete curvature calculation

To begin with, we quote the definition of curvature κ from [26], [28]. Let Γ be a regular planar curve which is parameterized by the arc length u (in mathematics, a planar curve is a curve in a plane that may be either a Euclidean planar, an affine planar, or a projective planar),

$$\Gamma(u) = (x(u), y(u)), \tag{1}$$

where $x(u)$ and $y(u)$ are coordinate functions and Γ is a discrete curve in Z^2. The curvature $\kappa(u)$ of the curve $\Gamma(u)$ is defined as follows

$$\kappa(u) = \frac{\dot{x}(u)\ddot{y}(u) - \ddot{x}(u)\dot{y}(u)}{(\dot{x}^2(u) + \dot{y}^2(u))^{3/2}}, \tag{2}$$

where $\dot{x}(u)$ and $\dot{y}(u)$ are first and $\ddot{x}(u)$ and $\ddot{y}(u)$ are second order derivatives with respect to u. The first and second order derivatives at a point $P_i = (x_i, y_i)$ ($P_i(x_i, y_i) \in Z^2$) on a curve are defined as

$$\dot{P}_i = \frac{P_{i+1} - P_{i-1}}{2}, \qquad \ddot{P}_i = \frac{\dot{P}_{i+1} - \dot{P}_{i-1}}{2}. \tag{3}$$

From Equation (3), it is easy to find that only one neighbouring point on each side of point P_i is used to estimate the first order derivative on P_i and only two neighbouring points on each side of point P_i are used to estimate the second order derivatives. This makes the estimation technique susceptible to the local variation on the curve and noise which may result in false detection.

To alleviate the influence of quantization errors, the curvature scale space technique [26], [28]–[32] is used for

corner detection. The single- or multi-scale Gaussian filters $g(u, \sigma)$ are used to smooth the curve. The curvature on the smoothed curve $\kappa(u, \sigma)$ is given as follows

$$\kappa(u, \sigma) = \frac{\dot{X}(u,\sigma)\ddot{Y}(u,\sigma) - \ddot{X}(u,\sigma)\dot{Y}(u,\sigma)}{(\dot{X}^2(u,\sigma) + \dot{Y}^2(u,\sigma))^{3/2}}, \quad (4)$$

where $\dot{X}(u,\sigma) = x(u) \otimes \dot{g}(u,\sigma)$, $\dot{Y}(u,\sigma) = y(u) \otimes \dot{g}(u,\sigma)$, $\ddot{X}(u,\sigma) = x(u) \otimes \ddot{g}(u,\sigma)$, $\ddot{Y}(u,\sigma) = y(u) \otimes \ddot{g}(u,\sigma)$. $\dot{g}(u,\sigma)$ is first and $\ddot{g}(u,\sigma)$ is second order derivative of $g(u,\sigma)$, and $\otimes$ is the convolution operator. It is indicated [33]–[39] that the conflict between corner detection and noise-sensitivity is irreconcilable with Gaussian smoothing.

It was indicated in [48], [49] that the existing discrete curvature calculation methods cannot accurately depict the difference between corners and edges. Fig. 1 depicts a corner model and the local variation of a curve in Fig. 1(a) and (b) respectively. In terms of Equations (2) and (3), the curvature at point o is $4/(5\sqrt{5})$ in Fig. 1(a) and $\sqrt{2}/2$ in Fig. 1(b). As a result, false corners may be detected based on the existing discrete curvature calculation.

Fig. 1 Examples of a corner model and the local variation of a curve. (a) A corner model, (b) Local variation of a curve.

B. Discrete curvature calculation

Our novel discrete curvature calculation is introduced as follows. The first and second order derivatives at a point P_i on a curve are defined as

$$\dot{P}_{i,d} = \frac{P_{i+d} - P_{i-d}}{2d}, \quad \ddot{P}_{i,d} = \frac{\dot{P}_{i+d} - \dot{P}_{i-d}}{2d}, \quad (5)$$

where d is the neighbouring distance on each side of point P_i. Consequently, the discrete curvature calculation in Equation (2) is given as follows

$$\kappa_d(u) = \frac{\dot{x}_d(u)\ddot{y}_d(u) - \ddot{x}_d(u)\dot{y}_d(u)}{(\dot{x}_d^2(u) + \dot{y}_d^2(u))^{3/2}}$$
$$= \frac{\psi(d)}{((x_{u+d} - x_{u-d})^2 + (y_{u+d} - y_{u-d})^2)^{3/2}}, \quad (6)$$

where

$$\psi(d) = (x_{u+d} - x_{u-d})((y_{u+2d} - y_u) - (y_u - y_{u-2d})) - \\ ((x_{u+2d} - x_u) - (x_u - x_{u-2d}))(y_{u+d} - y_{u-d}), \quad (7)$$

$\kappa_d(u)$ is a curvature function using neighbouring distance d, $\dot{x}_d(u)$ and $\dot{y}_d(u)$ are first and $\ddot{x}_d(u)$ and $\ddot{y}_d(u)$ are second order derivatives with respect to u using neighbouring distance d.

C. Discrete curvature representations

In this subsection, we will present the main result of this paper. The goal is to apply the discrete curvature Equation (6)

on the END model, STAIR model, and L model [26], [40] (as shown in Fig. 2) to derive the discrete curvature representations.

A universal END or STAIR corner model [26], which consists of two corner angles α and β and a distance w, is shown in Fig. 2(a) and (b) respectively. In terms of Equation (1), the END model can be written as

$$x(u) = \begin{cases} u\,\sin\alpha, & u < 0 \\ u, & 0 \le u < w \\ (u - w)\,\sin\beta, & w \le u, \end{cases}$$
$$y(u) = \begin{cases} u\,\cos\alpha, & u < 0 \\ 0, & 0 \le u < w \\ -(u - w)\,\cos\beta, & w \le u. \end{cases} \quad (8)$$

The two adjacent corners locate at $u = 0$ and $u = w$. The angle α is equal to 0 when the ray with $u < 0$ lies on the dashed line. The α $(\alpha > 0)$ increases when the ray turns clockwise and α $(\alpha < 0)$ decreases when the ray turns counter-clockwise. For the ray with $(u > w)$, the definition on β is just the opposite. Without loss of generality, it is assumed that $\alpha \in (-\pi/2, \pi/2)$. When $\beta \in (-\pi/2, \pi/2)$, it is an END model as shown in Fig. 2(a). When $\beta \in (\pi/2, 3\pi/2)$, it is a STAIR model as shown in Fig. 2(b). For ease of calculation, $\pi - \beta$ with $\beta \in (-\pi/2, \pi/2)$ is used in the STAIR model. When $\beta = \pi/2$, it is an L model as shown in Fig. 2(c).

From Fig. 2(a) and (b), it can be easily seen that if the curvatures of the two corners at the positions $u = 0$ and $u = w$ are larger than that at the midpoint $u = w/2$, the two adjacent corners can be separated and detected. For this reason, we focus on the discrete curvature representations of the three positions using Equation (6).

Representation 2.1 For the END corner model, two corners are separated by w $(w > 1)$ with $\alpha \in (-\pi/2, \pi/2)$ and $\beta \in (-\pi/2, \pi/2)$, and the discrete curvature representations at the positions $u = 0$, $u = w/2$, and $u = w$ are expressed as follows:

1) When $d \in [1, w/4)$, the discrete curvature representations are

$$\kappa_d(u)|_{u=0} = -\frac{\sqrt{2}}{d}\frac{\cos\alpha}{(1 + \sin\alpha)^{3/2}},$$
$$\kappa_d(u)|_{u=w/2} = 0, \quad (9)$$
$$\kappa_d(u)|_{u=w} = -\frac{\sqrt{2}}{d}\frac{\cos\beta}{(1 + \sin\beta)^{3/2}}.$$

2) When $d \in [w/4, w/2)$, the discrete curvature representations are

$$\kappa_d(u)|_{u=0} = -\frac{\sqrt{2}}{d}\frac{\cos\alpha}{(1 + \sin\alpha)^{3/2}},$$
$$\kappa_d(u)|_{u=w/2} = -\frac{(2d - w/2)(\cos\alpha + \cos\beta)}{4d^2}, \quad (10)$$
$$\kappa_d(u)|_{u=w} = -\frac{\sqrt{2}}{d}\frac{\cos\beta}{(1 + \sin\beta)^{3/2}}.$$

3) When $d \in [w/2, w)$, the discrete curvature representations are given by Equation (11).

4) When $d \in [w, +\infty)$, the discrete curvature representations are given by Equation (12).
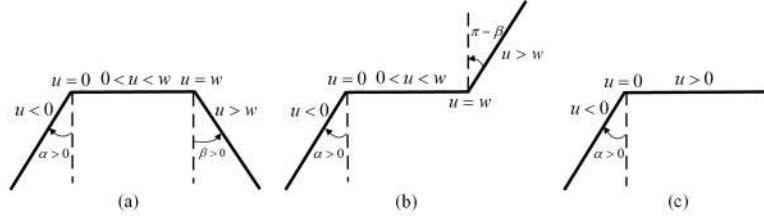
Fig. 2 Corner models: (a) END model, (b) STAIR model, (c) L model. The angles α and β can vary independently.

Representation 2.2 When $\pi - \beta$ is used instead of β with $\beta \in (-\pi/2, \pi/2)$, Equations (9)-(12) are the discrete curvature representations at the three positions $u = 0$, $u = w/2$, and $u = w$ for the STAIR model.

Representation 2.3 When $\beta = \pi/2$, Equations (9)-(12) are the discrete curvature representations at the three positions $u = 0$, $u = w/2$, and $u = w$ for the L model.

The discrete curvature representations indicate that the corner resolution of the corner models can be determined analytically, which allows us to derive properties from their representations. Meanwhile, we can easily determine from the discrete curvature representations whether the adjacent corners located at $u = 0$ and $u = w$ can be accurately detected or not. These are checked by the ranges of $\left|\kappa_d(u)_{|u=0}\right|$, $\left|\kappa_d(u)_{|u=w/2}\right|$, and $\left|\kappa_d(u)_{|u=w}\right|$ which vary when α, β, w, and d vary. Then only when the following inequality holds

$$\left|\kappa_d(u)_{|u=0}\right| > \left|\kappa_d(u)_{|u=w/2}\right|, \tag{13}$$

the two adjacent corners can be exactly detected. It is worth to note that the derivation process for $\left|\kappa_d(u)_{|u=w}\right| > \left|\kappa_d(u)_{|u=w/2}\right|$ is similar.

III. DISCRETE CURVATURE PROPERTIES OF CORNERS

In this subsection, the properties of the discrete curvature representations are investigated in detail about the effects of the corner angles α and β on the curvature representations. Next, the properties of the END, STAIR, and L models are presented.

A. END model

For the END model with $\alpha \in (-\pi/2, \pi/2)$ and $\beta \in (-\pi/2, \pi/2)$ in Equations (9)-(12), four cases are considered to investigate the properties of the discrete curvature representations and the detection of neighbouring corners.

1) When $d \in [1, w/4)$, in terms of Equation (9), it can be easily concluded that $\left|\kappa_d(u)_{|u=0}\right| > \left|\kappa_d(u)_{|u=w/2}\right|$. Then, the two adjacent corners can be easily detected.

2) When $d \in [w/4, w/2)$, in terms of Equation (10), inequality (13) becomes

$$\left|\frac{\sqrt{2}}{d}\frac{\cos\alpha}{(1+\sin\alpha)^{3/2}}\right| > \left|\frac{(2d-w/2)(\cos\alpha+\cos\beta)}{4d^2}\right|, \tag{14}$$

which can be written as

$$\frac{\cos\alpha}{(1+\sin\alpha)^{3/2}(\cos\alpha+\cos\beta)} > \frac{(2d-w/2)}{4\sqrt{2}d}. \tag{15}$$

The range of the right-hand side of inequality (15) is $\left[0, \frac{1}{4\sqrt{2}}\right)$. As a result, inequality (14) is established if it satisfies

$$\frac{\cos\alpha}{(1+\sin\alpha)^{3/2}(\cos\alpha+\cos\beta)} > \frac{1}{4\sqrt{2}}. \tag{16}$$

It can be seen that inequality (16) is nonlinear. The ranges on α and β which satisfy inequality (16) is shown in Fig. 3(a). The white area indicates that inequality (16) is established. Then the neighbouring corners can be accurately detected. On the contrary, the gray area indicates that inequality (16) does not hold. Subsequently, the adjacent corners cannot be accurately

$$
\begin{aligned}
\kappa_d(u)_{|u=0} &= -\frac{(2d+w)\cos\alpha + (2d-w)\sin(\alpha+\beta) + (2d-w)\cos\beta}{d^2(1+\sin\alpha)^{3/2}}, \\
\kappa_d(u)_{|u=w/2} &= -\frac{(2d-w/2)((2d-w)\sin(\alpha+\beta) + w(\cos\alpha+\sin\beta))}{((d-w/2)^2(2-2\cos(\alpha+\beta)) + w(2d-w)(\sin\alpha+\sin\beta) + w^2)^{3/2}}, \\
\kappa_d(u)_{|u=w} &= -\frac{(2d+w)\cos\beta + (2d-w)\sin(\alpha+\beta) + (2d-w)\cos\alpha}{d^2(1+\sin\beta)^{3/2}}.
\end{aligned}
\tag{11}
$$

$$
\begin{aligned}
\kappa_d(u)_{|u=0} &= -\frac{d(3w\cos\alpha + (4d-3w)\sin(\alpha+\beta) + w\cos\beta)}{(2d^2(1-\cos(\alpha+\beta)) + 2w^2(1-\sin\beta) + 2dw(\sin\alpha+\sin\beta+\cos(\alpha+\beta)-1))^{3/2}}, \\
\kappa_d(u)_{|u=w/2} &= -\frac{(2d-w/2)((2d-w)\sin(\alpha+\beta) + w(\cos\alpha+\sin\beta))}{((d-w/2)^2(2-2\cos(\alpha+\beta)) + w(2d-w)(\sin\alpha+\sin\beta) + w^2)^{3/2}}, \\
\kappa_d(u)_{|u=w} &= -\frac{d(3w\cos\beta + (4d-3w)\sin(\alpha+\beta) + w\cos\alpha)}{(2d^2(1-\cos(\alpha+\beta)) + 2w^2(1-\sin\alpha) + 2dw(\sin\alpha+\sin\beta+\cos(\alpha+\beta)-1))^{3/2}}.
\end{aligned}
\tag{12}
$$

detected, which may lead to false corner detection.

3) When $d \in [w/2, w)$, in terms of Equation (11), inequality (13) can be rewritten as inequality (17). The inequality (17) is established if it satisfies

$$\frac{\cos\alpha \left(\frac{\cos(\frac{\alpha-\beta}{2}) + \sin(\frac{\alpha+\beta}{2})}{2\cos(\frac{\alpha-\beta}{2}) + \sin(\frac{\alpha+\beta}{2})} \cos(\frac{\alpha-\beta}{2}) \right)^{1/2}}{(1+\sin\alpha)^{3/2}\cos(\frac{\alpha+\beta}{2}) \left| \sin^{-3/2}(\frac{\alpha-\beta}{2}) \right|} > \frac{3\sqrt{2}}{4}. \quad (18)$$

See Appendix A for more details. The ranges on α and β which satisfy inequality (18) are shown in Fig. 3(b).

4) When $d \in [w, +\infty)$, in terms of Equation (12), inequality (13) can be rewritten as inequality (19). It is worth to note that $\lim\limits_{d\to+\infty} |\kappa_d(u)_{|u=0}| = \lim\limits_{d\to+\infty} |\kappa_d(u)_{|u=w/2}|$. Therefore, inequality $|\kappa_d(u)_{|u=0}| > |\kappa_d(u)_{|u=w/2}|$ does not hold when $d \to +\infty$. The same applies to the STAIR and L models. Then we investigate the discrete curvature properties in the case $d \in [w, \tau w]$ with $\tau > 1$ and $\tau \ll +\infty$. Inequality (19) is established when it satisfies the followings:

a) With $\frac{\alpha+\beta}{2} \in \left(-\frac{\pi}{2}, \arcsin\left(-\frac{w(3\cos\alpha+\cos\beta)}{2(4d-3w)\cos(\frac{\alpha+\beta}{2})} \right) \right)$,

$$-\frac{(4-\frac{3}{\tau})\sin(\alpha+\beta) + \frac{3}{\tau}\cos\alpha + \frac{1}{\tau}\cos\beta}{\left(\sin^2(\frac{\alpha+\beta}{2}) + \frac{1}{\tau^2}\sin^2(\frac{\pi}{4}-\frac{\beta}{2}) \right)^{3/2}}$$
$$> \frac{4\sqrt{2}\tau^{3/2}(2-\frac{1}{2\tau})\cos(\frac{\alpha+\beta}{2})}{\left| (2-\frac{1}{\tau})\sin(\frac{\alpha+\beta}{2}) + \frac{1}{\tau}\cos(\frac{\alpha-\beta}{2}) \right|^{1/2} \left| \sin^{\frac{3}{2}}(\frac{\alpha-\beta}{2}) \right|}. \quad (20)$$

b) With $\frac{\alpha+\beta}{2} \in \left(\arcsin\left(-\frac{w(3\cos\alpha+\cos\beta)}{2(4d-3w)\cos(\frac{\alpha+\beta}{2})} \right), 0 \right)$,

$$\frac{(4-\frac{3}{\tau})\sin(\alpha+\beta) + \frac{3}{\tau}\cos\alpha + \frac{1}{\tau}\cos\beta}{\left(\sin^2(\frac{\alpha+\beta}{2}) + \frac{1}{\tau^2}\sin^2(\frac{\pi}{4}-\frac{\beta}{2}) \right)^{3/2}}$$
$$> \frac{4\sqrt{2}\tau^{3/2}(2-\frac{1}{2\tau})\cos(\frac{\alpha+\beta}{2})}{\left| (2-\frac{1}{\tau})\sin(\frac{\alpha+\beta}{2}) + \frac{1}{\tau}\cos(\frac{\alpha-\beta}{2}) \right|^{1/2} \left| \sin^{3/2}(\frac{\alpha-\beta}{2}) \right|}. \quad (21)$$

c) With $\frac{\alpha+\beta}{2} \in \left[0, \frac{\pi}{2} \right)$,

$$\frac{(4-\frac{3}{\tau})\sin(\alpha+\beta) + \frac{3}{\tau}\cos\alpha + \frac{1}{\tau}\cos\beta}{\left(\sin(\frac{\alpha+\beta}{2}) + \frac{1}{\tau}\sin(\frac{\pi}{4}-\frac{\beta}{2}) \right)^3}$$
$$> \frac{4\sqrt{2}\tau^{3/2}(2-\frac{1}{2\tau})\cos(\frac{\alpha+\beta}{2})}{\left((2-\frac{1}{\tau})\sin(\frac{\alpha+\beta}{2}) + \frac{1}{\tau}\cos(\frac{\alpha-\beta}{2}) \right)^{1/2} \left| \sin^{3/2}(\frac{\alpha-\beta}{2}) \right|}. \quad (22)$$

See Appendix B for more details. The ranges on α and β which satisfy inequality (19) for case 4 of the END model with $\tau = 1.3$ and $\tau = 2$ are shown in Fig. 3(c) and (d) respectively.
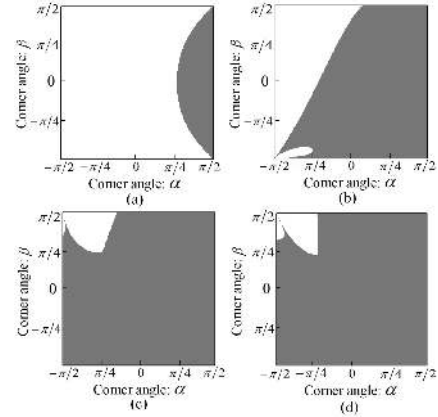

Fig. 3 The ranges on α and β which satisfy inequality (13) of the END model with different d: (a) $d \in [w/4, w/2)$, (b) $d \in [w/2, w)$, (c) $\tau = 1.3$, and (d) $\tau = 2$.

Property 3.1 For the END corner model, two corners are separated by w ($w > 1$) with $\alpha \in (-\pi/2, \pi/2)$ and $\beta \in (-\pi/2, \pi/2)$. The region for α and β in which the corners can be detected becomes smaller as d increases.

B. STAIR model

When $\pi - \beta$ is used instead of β with $\beta \in (-\pi/2, \pi/2)$, Equations (9)-(12) are the discrete curvature representations at the three positions $u = 0$, $u = w/2$, and $u = w$ for the STAIR model. Subsequently, we investigate the properties of the curvatures at two positions $u = 0$ and $u = w/2$. If the

$$\left| \frac{(2d+w)\cos\alpha + (2d-w)\sin(\alpha+\beta) + (2d-w)\cos\beta}{d^2(2+2\sin\alpha)^{3/2}} \right|$$
$$> \left| \frac{(2d-w/2)((2d-w)\sin(\alpha+\beta) + w(\cos\alpha+\cos\beta))}{((d-w/2)^2(2-2\cos(\alpha+\beta)) + w(2d-w)(\sin\alpha+\sin\beta) + w^2)^{3/2}} \right|. \quad (17)$$

$$\left| \frac{d(3w\cos\alpha + (4d-3w)\sin(\alpha+\beta) + w\cos\beta)}{(2d^2(1-\cos(\alpha+\beta)) + 2w^2(1-\sin\beta) + 2dw(\sin\alpha+\sin\beta+\cos(\alpha+\beta)-1))^{3/2}} \right|$$
$$> \left| \frac{(2d-w/2)((2d-w)\sin(\alpha+\beta) + w(\cos\alpha+\cos\beta))}{((d-w/2)^2(2-2\cos(\alpha+\beta)) + w(2d-w)(\sin\alpha+\sin\beta) + w^2)^{3/2}} \right|. \quad (19)$$

curvature satisfies with inequality (13), the adjacent corners can be exactly detected. Four cases are considered.

1) When $d \in [1, w/4)$, in terms of Equation (9), it can be easily concluded that $\left|\kappa_d(u)_{|u=0}\right| > \left|\kappa_d(u)_{|u=w/2}\right|$. As a result, the two adjacent corners can be easily detected.

2) When $d \in [w/4, w/2)$, in terms of Equation (10), inequality (13) becomes

$$\left|\frac{\sqrt{2}}{d}\frac{\cos\alpha}{(1+\sin\alpha)^{3/2}}\right| > \left|\frac{(2d-w/2)(\cos\alpha-\cos\beta)}{4d^2}\right|, \quad (23)$$

which can be written as

$$\frac{\cos\alpha}{(1+\sin\alpha)^{3/2}|\cos\alpha-\cos\beta|} > \frac{(2d-w/2)}{4\sqrt{2}d}. \quad (24)$$

The range of the right-hand side of inequality (24) is $\left[0, \frac{1}{4\sqrt{2}}\right)$. Then inequality (24) is established if it satisfies

$$\frac{\cos\alpha}{(1+\sin\alpha)^{3/2}} > \frac{|\cos\alpha-\cos\beta|}{4\sqrt{2}}. \quad (25)$$

The ranges on α and β which satisfy inequality (25) is shown in Fig. 4(a).

3) When $d \in [w/2, w)$, in terms of Equation (11), inequality (13) can be rewritten as inequality (26). The inequality (26) is established if it satisfies the followings:

a) With $\frac{\beta-\alpha}{2} \in \left(-\frac{\pi}{2}, \arctan\left(-\frac{w}{2d}\arctan(\frac{\pi}{4}-\frac{\beta}{2})\right)\right)$,

$$\xi(\alpha,\beta)\left(\cos^2\left(\frac{\beta-\alpha}{2}\right)+\sin^2\left(\frac{\pi}{4}-\frac{\beta}{2}\right)\sin^2\left(\frac{\pi}{4}-\frac{\alpha}{2}\right)\right)$$
$$> 4\xi(\alpha,\beta)\cos\left(\frac{\beta-\alpha}{2}\right)\sin\left(\frac{\pi}{4}-\frac{\beta}{2}\right)\sin\left(\frac{\pi}{4}-\frac{\alpha}{2}\right)$$
$$+ \frac{3}{4}\left|\sin\left(\frac{\beta-\alpha}{2}\right)\right|\cos^2\left(\frac{\pi}{4}-\frac{\alpha}{2}\right), \quad (27)$$

where

$$\xi(\alpha,\beta) = \left|\sin\left(\frac{\beta-\alpha}{2}\right)\right|\cos\left(\frac{\pi}{4}-\frac{\beta}{2}\right) \\ - \cos\left(\frac{\beta-\alpha}{2}\right)\sin\left(\frac{\pi}{4}-\frac{\beta}{2}\right). \quad (28)$$

b) With $\frac{\beta-\alpha}{2} \in \left(\arctan\left(-\frac{w}{2d}\arctan(\frac{\pi}{4}-\frac{\beta}{2})\right), \frac{\pi}{2}\right)$,

$$\psi(\alpha,\beta)\left(\cos^2\left(\frac{\beta-\alpha}{2}\right)+\sin^2\left(\frac{\pi}{4}-\frac{\beta}{2}\right)\sin^2\left(\frac{\pi}{4}-\frac{\alpha}{2}\right)\right)$$
$$> 4\psi(\alpha,\beta)\cos\left(\frac{\beta-\alpha}{2}\right)\sin\left(\frac{\pi}{4}-\frac{\beta}{2}\right)\sin\left(\frac{\pi}{4}-\frac{\alpha}{2}\right)$$
$$+ \frac{3}{2}\left|\sin\left(\frac{\beta-\alpha}{2}\right)\right|\cos^2\left(\frac{\pi}{4}-\frac{\alpha}{2}\right), \quad (29)$$

where

$$\psi(\alpha,\beta) = 2\sin\left(\frac{\beta-\alpha}{2}\right)\cos\left(\frac{\pi}{4}-\frac{\beta}{2}\right) \\ + \cos\left(\frac{\beta-\alpha}{2}\right)\sin\left(\frac{\pi}{4}-\frac{\beta}{2}\right). \quad (30)$$

See Appendix C for more details. The ranges on α and β which satisfy case 3 of the STAIR model is shown in Fig. 4(b).

4) When $d \in [w, \tau w]$, in terms of Equation (12), inequality (13) can be rewritten as inequality (31). Inequality (31) is established when it satisfies the followings:

a) With $\frac{\beta-\alpha}{2} \in \left(-\frac{\pi}{2}, \arcsin\left(\frac{-w\cos\alpha}{4(d-w)\cos(\frac{\beta-\alpha}{2})+2w\cos(\frac{\pi}{4}-\frac{\alpha}{2})\cos(\frac{\pi}{4}-\frac{\beta}{2})}\right)\right)$,

$$-\frac{(4-\frac{3}{\tau})\sin(\beta-\alpha)+\frac{3}{\tau}\cos\alpha-\frac{1}{\tau}\cos\beta}{\left(4\cos^2(\frac{\beta-\alpha}{2})+\frac{4}{\tau^2}\cos^2(\frac{\pi}{4}+\frac{\beta}{2})\right)^{3/2}}$$
$$> \frac{2(2-\frac{1}{2\tau})\left|\sin(\frac{\beta-\alpha}{2})\right|}{\left((2-\frac{1}{\tau})\cos(\frac{\beta-\alpha}{2})+\frac{1}{\tau}\sin(\frac{\alpha+\beta}{2})\right)^2}. \quad (32)$$

b) With $\frac{\beta-\alpha}{2} \in \left(\arcsin\left(\frac{-w\cos\alpha}{4(d-w)\cos(\frac{\beta-\alpha}{2})+2w\cos(\frac{\pi}{4}-\frac{\alpha}{2})\cos(\frac{\pi}{4}-\frac{\beta}{2})}\right), \frac{\pi}{2}\right)$,

$$\frac{(4-\frac{3}{\tau})\sin(\beta-\alpha)+\frac{3}{\tau}\cos\alpha-\frac{1}{\tau}\cos\beta}{\left(4\cos^2(\frac{\beta-\alpha}{2})+\frac{4}{\tau^2}\cos^2(\frac{\pi}{4}+\frac{\beta}{2})\right)^{3/2}}$$
$$> \frac{2(2-\frac{1}{2\tau})\left|\sin(\frac{\beta-\alpha}{2})\right|}{\left((2-\frac{1}{\tau})\cos(\frac{\beta-\alpha}{2})+\frac{1}{\tau}\sin(\frac{\alpha+\beta}{2})\right)^2}. \quad (33)$$

See Appendix D for more details. The ranges on α and β which satisfy case 4 of the STAIR model with $\tau = 1.3$ and $\tau = 2$ are shown in Fig. 4(c) and (d) respectively.

$$\left|\frac{(2d-w)(\cos\alpha-\cos\beta+\sin(\beta-\alpha))+2w\cos\alpha}{d^2(2+2\sin\alpha)^{3/2}}\right| \\ > \left|\frac{(2d-w/2)((2d-w)\sin(\beta-\alpha)+w(\cos\alpha-\cos\beta))}{((d-w/2)^2(2+2\cos(\beta-\alpha))+w(2d-w)(\sin\alpha+\sin\beta)+w^2)^{3/2}}\right|. \quad (26)$$

$$\left|\frac{d(3w\cos\alpha+(4d-3w)\sin(\beta-\alpha)-w\cos\beta)}{(2d^2(1+\cos(\beta-\alpha))+2w^2(1-\sin\beta)+2dw(\sin\alpha+\sin\beta-\cos(\beta-\alpha)-1))^{3/2}}\right| \\ > \left|\frac{(2d-w/2)((2d-w)\sin(\beta-\alpha)+w(\cos\alpha-\cos\beta))}{((d-w/2)^2(2+2\cos(\beta-\alpha))+w(2d-w)(\sin\alpha+\sin\beta)+w^2)^{3/2}}\right|. \quad (31)$$
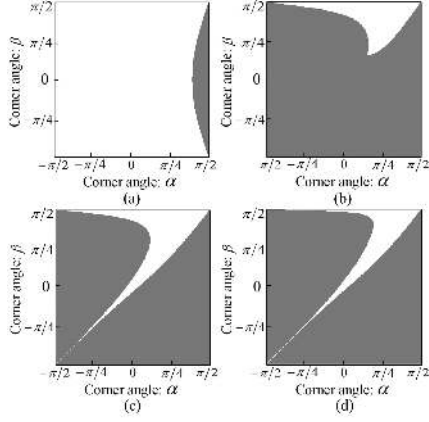
Fig. 4 The ranges on α and β which satisfy inequality (13) of the STAIR model with different d: (a) $d \in [w/4, w/2)$, (b) $d \in [w/2, w)$, (c) $\tau = 1.3$, and (d) $\tau = 2$.

Property 3.2 For the STAIR corner model, two corners are separated by w ($w > 1$) with $\alpha \in (-\pi/2, \pi/2)$ and $\beta \in (-\pi/2, \pi/2)$. The region for α and β in which the corners can be detected becomes smaller as d increases.

C. L model

When $\alpha \in (-\pi/2, \pi/2)$ and $\beta = \pi/2$, Equations (9)-(12) are the discrete curvature representations at the three positions $u = 0$, $u = w/2$, and $u = w$ for the L model. It follows that we only need to investigate the properties for the curvatures at two positions $u = 0$ and $u = w/2$. If the curvature satisfies with inequality (13), the adjacent corners can be exactly detected. Four cases are considered.

1) When $d \in [1, w/4)$, in terms of Equation (9), it can be easily concluded that $\left|\kappa_d(u)_{|u=0}\right| > \left|\kappa_d(u)_{|u=w/2}\right|$. Subsequently, the corner at the position $u = 0$ can be exactly detected.

2) When $d \in [w/4, w/2)$, in terms of Equation (10), inequality (13) becomes

$$\left|\frac{\sqrt{2}}{d}\frac{\cos\alpha}{(1+\sin\alpha)^{3/2}}\right| > \left|\frac{(2d-w/2)\cos\alpha}{4d^2}\right|, \quad (34)$$

which can be rewritten as

$$\frac{1}{(1+\sin\alpha)^{3/2}} > \frac{(2d-w/2)}{4\sqrt{2}d}. \quad (35)$$

The range of the right-hand side of inequality (35) is $\left[0, \frac{1}{4\sqrt{2}}\right)$. It is very easy to prove that inequality (35) is established. Then it can be concluded that the corner at the position $u = 0$ can be exactly detected in this case.

3) When $d \in [w/2, w)$, in terms of Equation (11), inequality (13) becomes

$$\frac{\sqrt{2}\cos\alpha}{d(1+\sin\alpha)^{3/2}} > \frac{2d(2d-w/2)\cos\alpha}{((2d^2-w^2/2)(1+\sin\alpha)+w^2)^{3/2}}, \quad (36)$$

which can be rewritten as

$$\left(\left(2-\left(\frac{w}{\sqrt{2}d}\right)^2\right)+\frac{(w/d)^2}{1+\sin\alpha}\right)^{3/2} > \sqrt{2}\left(2-\frac{w}{2d}\right). \quad (37)$$

It is easy to prove that inequality (37) is established. Then it can be concluded that the corner at the position $u = 0$ can be exactly detected in this case.

4) When $d \in [w, \tau w]$, in terms of Equation (12), inequality (13) can be rewritten as

$$\frac{\sqrt{2}\cos\alpha}{d(1+\sin\alpha)^{3/2}} > \frac{2d(2d-w/2)\cos\alpha}{((2d^2-w^2/2)(1+\sin\alpha)+w^2)^{3/2}}. \quad (38)$$

Inequality (38) can be rewritten as

$$\left((2\tau^2-1/2)+\frac{1}{1+\sin\alpha}\right)^{3/2} > \sqrt{2}\tau^2(2\tau-1/2). \quad (39)$$

It is easy to prove that inequality (39) is established. Then it can be concluded that the corner at the position $u = 0$ can be exactly detected in this case.

Property 3.3 For the L corner model, the corner with $\alpha \in (-\pi/2, \pi/2)$ can always be exactly detected as d increases.

IV. NEW CORNER DETECTION METHOD

In this section, the corner resolution based on the proposed discrete curvature representation is investigated, and its corresponding corner resolution constant is derived. Furthermore, the properties of the discrete curvature representations are used to construct a new corner measure and a new corner detection method is proposed.

A. Corner resolution

Corner resolution is defined as the capability of a corner measure to differentiate nearby corners. The ability of the curvature representation technique to detect adjacent corners depends on whether the curvature maxima of the adjacent corners can be resolved.

For the END and STAIR models, two corners are separated by w ($w > 1$) with $\alpha \in (-\pi/2, \pi/2)$ and $\beta \in (-\pi/2, \pi/2)$. In terms of discrete curvature representation, only if d is less than $w/4$, the adjacent corners can be exactly detected without considering angle change. It means, given a d, only if the distance w between the adjacent corners is larger than $4d$, the adjacent corners can be exactly detected. Then the corner resolution constant λ can be defined as $\lambda = 4d - 1$. For example $d = 1$, the corresponding corner resolution constant is $\lambda = 3$; with $d = 2$, λ is 7; and with $d = 3$, λ is 11.

B. New corner measure

Based on the above analysis, we can conclude that curvature calculation for a corner measure using a small d has good corner localization and good ability to resolve adjacent corners but is noise-sensitive. Taking the existing discrete curvature calculation technique as an example, $d=1$ is used to calculate the curvature and detect corners in [26], [28]. The two methods [26], [28] have the highest corner resolution ($\lambda = 3$) in the existing contour-based methods [4], [26]–[42]. However, the two methods [26], [28] are sensitive to local variations and cannot accurately depict the difference between corners and edges, as shown in Fig. 1. Curvature calculation for a corner measure using a large d is noise-robust but it will degrade corner resolution.

To obtain better corner detection accuracy with a high corner resolution and noise robustness simultaneously, a new corner measure is proposed in this paper with curvature calculation given as

$$
\begin{aligned}
\Lambda(u) = & \frac{|\dot{x}_{d_1}(u)\ddot{y}_{d_1}(u) - \ddot{x}_{d_1}(u)\dot{y}_{d_1}(u)|}{(\dot{x}_{d_1}^2(u) + \dot{y}_{d_1}^2(u))^{3/2}} \times \\
& \frac{|\dot{x}_{d_2}(u)\ddot{y}_{d_2}(u) - \ddot{x}_{d_2}(u)\dot{y}_{d_2}(u)|}{(\dot{x}_{d_2}^2(u) + \dot{y}_{d_2}^2(u))^{3/2}},
\end{aligned} \tag{40}
$$

where $d_1 = 2$ and $d_2 = 3$. For the END and STAIR models, provided that two corners are separated by $w = 8$ with $\alpha \in (-\pi/2, \pi/2)$ and $\beta \in (-\pi/2, \pi/2)$, it can be easily found from Equation (40) that the curvature $\Lambda(u)_{|u=4}$ is 0. It means that the two adjacent corners can be exactly detected. From the above analysis, $\lambda = 7$ pixels can be used to represent the corner resolution of the proposed new corner measure for two neighbouring corners. This is defined as the corner resolution constant of the proposed corner measure. In corner detection, the detection of neighbouring corners is mainly determined by the corner resolution constant.

In general, the above curvature function has the following advantages over the existing contour-based corner detection techniques [26], [28], [29], [31], [34], [36]–[38]. For a curvature-based corner measure, noise-robustness usually means poor corner localization because of large scale Gaussian smoothing. The proposed corner measure has a high corner resolution using a small d_1 while maintaining high noise-robustness using a large d_2, which also enhances the stability of corner detection and avoids the degradation of corner localization. This is impossible for the existing contour-based corner detectors [26], [28]–[31] using the multi-scale curvature techniques [26]. The proposed corner measure makes corners more distinguishable and suppresses false corners effectively, and it also avoids the issue of parameter selection for an appropriate Gaussian smoothing scale. As a result, false corner detections are less likely to occur.

C. Comparisons of corner measures

In what follows, we compare our new corner measure with the MSCP measure [29], the local curvature measure [31], the CPDA measure [34], the local curvature measure using Equation (5) ($d=2$), and the local curvature measure using Equation (5) ($d=3$) for the contour-based corner detectors. Fig. 5 illustrates the test image 'Block', edge contours extracted by the Canny edge detector [50], the MSCP measure [29], the local curvature measure [31], the CPDA measure [34], the local curvature measure using Equation (5) ($d=2$), the local curvature measure using Equation (5) ($d=3$), and the new corner measure on the contour. One example edge contour is extracted from the edge map indicated by the arrow in Fig. 5(b), which contains 13 corners labelled by the black squares in Fig. 5(c). The three other corner measures use the default choices in their original codes and the 13 corners in the contour match 13 peaks of the four graphs. It can be observed that the six graphs in Fig. 5(d)-(i) demonstrate different behaviours. The MSCP measure [31] uses three different scales to smooth the edge contour, and then the product of the three corresponding curvatures via Equation (2) is defined as the corner measure, which has the ability to suppress local variations. However, the fusion of multi-scale curvatures from different smoothed edge contours may lead to the difficulty in extracting some candidate corners from the edge contour, for example, the sixth and ninth candidate corners as shown in Fig. 5(d). This implies that the MSCP detector has a large probability of occurrence for missing corners. The local curvature measure in [31] uses a single scale of Gaussian to smooth the edge contour and to calculate the curvature for corner detection. This measure contains some maxima with larger magnitudes besides the 13 corners, meaning that the detector [31] has a slightly large probability of generating false corners. The CPDA corner measure has hardly any maximum besides the corners, implying that the CPDA detector has a small probability of generating false corners. However, the CPDA detector might potentially miss obvious corners where two neighbouring candidate corners are located close to each other, just as the sixth candidate corner which has the fifth corner nearby, as shown in Fig. 5(f). The reason is that the chord length with more number of pixels is used to calculate the chord-to-point distance [38], [39], which affect the calculation of curvatures. The local curvature measures using Equation (5) ($d=2$ or $d=3$) contain some maxima with larger magnitudes besides the 13 corners. This implies that the local curvature measures using Equation (5) ($d=2$ or $d=3$) have a slightly large probability of generating false corners. Our new corner measure has sharp peaks at corners and almost no local maxima apart from the 13 corners. This means that the new corner measure is better in corner detection and has the ability to resolve adjacent corners on a contour than the three other detectors [29], [31], [34].

D. Contour-based corner detection using new corner measure

In this section, we describe how our proposed corner measure described above is used in our proposed detector. The proposed corner detector first extracts the edge map from an input image using the Canny edge detector [50]. Consequently, planar curves are extracted from the edge map. Next, Equation (40) is used to estimate the curvature on the curves. The local maxima of the curvatures along the curves are marked as candidate corners. Finally, a single curvature threshold is used to select corners.

The outline of the proposed corner detection algorithm is as follows:

1) Detect edges from the input image using Canny or other edge detectors to obtain a binary edge map.
2) Extract contours from the edge map as in the methods of [28], [31]:
   - Fill in gaps along the edge contours.
   - Locate the T-junctions and mark them as T-corners.
3) For each point of the contours, calculate the curvature following the proposed corner measure as in Equations (40).
4) Find the local maxima of curvature as candidate corners and remove false corners by comparing with the curvature threshold T_h.
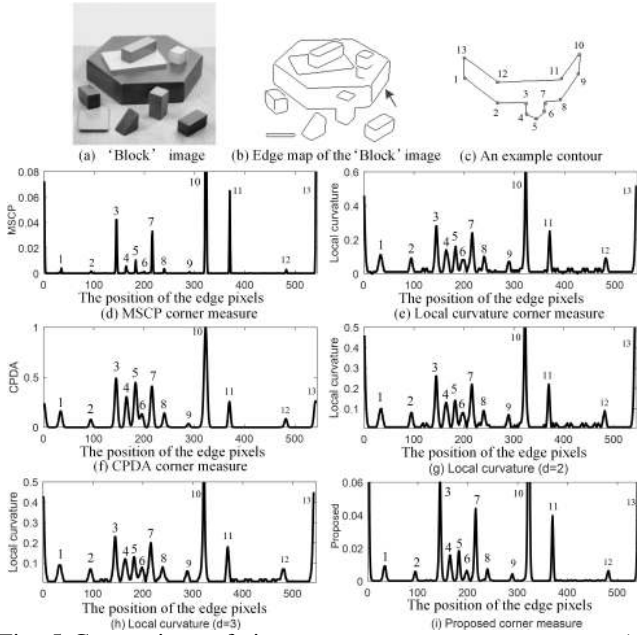
Fig. 5 Comparison of six corner measures on a contour, (a) Noise-free 'Block' image, (b) Edge map, (c) A closed contour with 13 corners, (d) The MSCP corner measure in [29], (e) Local curvature measure in [31], (f) The CPDA measure in [34], (g) Local curvature measure using Equation (5) (d=2), (h) Local curvature measure using Equation (5) (d=3), and (i) Proposed corner measure on the contour.

V. EXPERIMENTAL RESULTS AND PERFORMANCE EVALUATION

The full performance evaluation on the proposed corner detector is reported in this section. Firstly, three images with ground truths are used to compare the proposed method with seven state-of-the-art corner detectors (MSCP [29], He & Yung [31], CPDA [34], ARCSS [35], GCM [36], ANDD [5], and ADCC [42]) in terms of the numbers of missed and false corners and localization errors of correctly detected corners [5], [38]. Secondly, 24 images are used to evaluate the detectors' average repeatability under image affine transformations, JPEG compression, and noise degradation.

The three commonly used test images 'Block', 'Lab' and 'Pentagon' [5], [31] are used in one of the performance evaluations [5], [31], [39]. The ground truths of the three test images are shown in Fig. 6(a), (b) and (c). In the three ground truth images, the image 'Block' contains 59 corners, the image 'Lab' contains 249 corners, and the image 'Pentagon' contains 78 corners. It is worth to note that 'Block' and 'Lab' are noise free images, while 'Pentagon' is a natural image with noise.

Let $DC = \{(\hat{x}_i, \hat{y}_i), i = 1, 2, \ldots, M_1\}$ and $GT = \{(x_j, y_j), j = 1, 2, \ldots, M_2\}$ be the detected corners by a corner detector and the true corners in the ground truth images respectively. For a corner (x_j, y_j) in set GT, we find its minimal distance from set DC. If the minimal distance is not more than the predefined threshold δ (here $\delta = 4$), the corner (x_j, y_j) is treated as correctly detected. Consequently, corner (x_j, y_j) in set GT and the detected corner in set
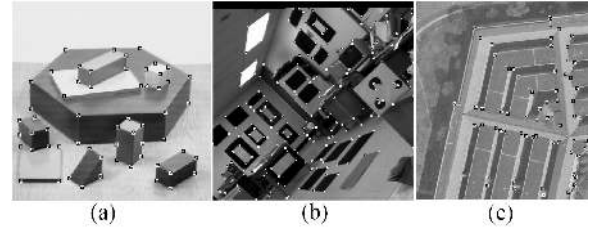

Fig. 6 Test images (a) 'Block', (b) 'Lab', and (c) 'Pentagon' and their ground truth corner positions.

DC form a matched pair. Otherwise, the corner (x_j, y_j) is counted as a missed corner. Similarly, for a corner $(\hat{x}_i, \hat{y}_i)$ in set DC, we find its minimal distance from set GT. If the minimal distance is larger than threshold δ, then corner $(\hat{x}_i, \hat{y}_i)$ is labelled as a false corner. The localization error is defined as the average distance on all the matched pairs. Let $\{(\hat{x}_k, \hat{y}_k), (x_k, y_k): k = 1, 2, \ldots, N\}$ be the matched corner pairs in sets GT and DC. As a result, the average localization error is calculated by

$$AL_e = \sqrt{\frac{1}{N}\sum_{k=1}^{N}((\hat{x}_k - x_k)^2 + (\hat{y}_k - y_k)^2)}. \tag{41}$$

It is worth to note that the predefined δ is determined by the corner resolution constant. In this paper, the corner resolution constant λ is 7, so it is right to set $\delta = 4$.

The seven other detectors [5], [29], [31], [34]–[36], [42] use the authors' original codes. Here, the default values are used for all the tuneable parameters of the detectors. The parameter settings for the proposed detector are: two lengths of curvature calculation $d_1 = 2$ and $d_2 = 3$, the thresholds for Canny edge detector being $low = 0$ and $high = 0.35$, and the curvature threshold $T_h = 0.008$. The choices for the thresholds of the Canny edge detector are based on methods in [31], [36], [39]. The parameter settings are taken in the set

$$\left\{ \begin{array}{l} d_1 = 1, 2, 3; \\ d_2 = 2, 3, 4; \ (d_2 > d_1) \\ T_h = 0.001, 0.0015, ..., 0.0325 \end{array} \right\}. \tag{42}$$

Below we discuss how the parameters (d_1, d_2, and T_h) for the proposed method are selected.

Assuming that missing a corner and reporting a false corner incur the same loss for detection performance, we use the total of missed and false corners to evaluate the detection performance for the proposed method. For the three test images, the effect of parameter changes on the proposed corner detector is shown in Fig. 7. It can be observed that the proposed detector with $d_1 = 2$, $d_2 = 3$, and $T_h = 0.008$ (marked by '∘') achieves a better detection accuracy than the proposed detector with other parameter settings.

As the number of test images with ground truths are limited, it is not sufficient to evaluate the performance of the corner detectors just based on these images. For important applications such as feature matching and registration, the average repeatability under affine transformations, JPEG compression, and noise degradation was suggested [5], [34], [38], [39] for the evaluation of corner detectors. Repeatability
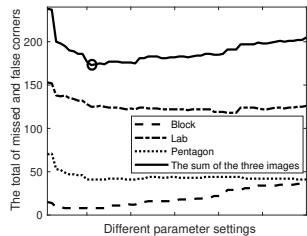
Fig. 7 Effect of parameters changes on the proposed corner detector.

computation does not require the ground truths of images. Therefore, a large image dataset can be used for evaluation.

In [34], the average repeatability R_{avg} explicitly measures the geometrical stability of the detected corners based on the original and affine transformed images. It is defined as:

$$R_{avg} = \frac{N_r}{2}\left(\frac{1}{N_o} + \frac{1}{N_t}\right),\tag{43}$$

where N_o and N_t represent the number of detected corners from the original and transformed images by a detector, and N_r is the number of corners between them. It is noted that a corner point $B_i = (x_i, y_i)$ is detected in the original image and its corresponding position is point Q_j after geometric image transformation. If a corner point is detected in a geometrically transformed image, and it is in the neighbourhood of Q_j (say within 4 pixels which is also determined by the corner resolution constant of the proposed corner measure), then a repeated corner is achieved. A higher average repeatability means a better performance.

A. Evaluation of detection performance based on ground truth images

In the first experiment, we compare the eight detectors using three images with ground truths. The detection results of the seven detectors are given in Fig. 8, Fig. 9, and Fig. 10. The number of missed corners, the number of false corners, and the localization error for each detector are listed in Table I.
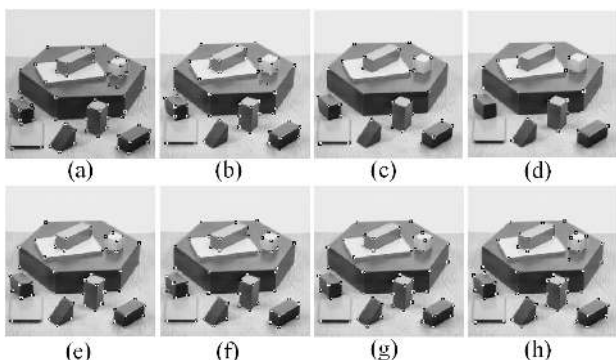

Fig. 8 Detection results on the test image 'Block'. (a) MSCP detector [29], (b) He & Yung detector [31], (c) CPDA detector [34], (d) ARCSS detector [35], (e) GCM detector [36], (f) ANDD detector [5], (g) ADCC detector [42], and (h) Proposed detector.

In this experiment, the total numbers of missed and false corners are used to evaluate the detection performance for
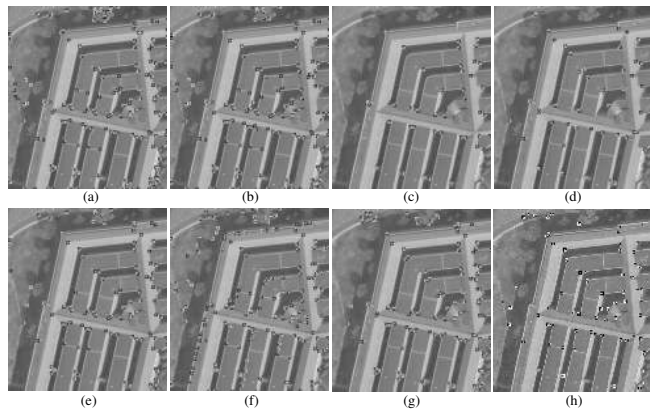

Fig. 10 Detection results on the test image 'Pentagon'. (a) MSCP detector [29], (b) He & Yung detector [31], (c) CPDA detector [34], (d) ARCSS detector [35], (e) GCM detector [36], (f) ANDD detector [5], (g) ADCC detector [42], and (h) Proposed detector.

a corner detector. Furthermore, considering the number of true corners in the three test images, the ratio of the total number of missed and false corners to the number of true corners in the ground truths can be used to quantitatively evaluate the detection performance. For the three test images, the ratios for the eight corner detectors, i.e., MSCP [29], He & Yung [31], CPDA [34], ARCSS [35], GCM [36], ANDD [5], ADCC [42], and the proposed detector are 237/386, 219/386, 207/386, 276/386, 176/386, 261/386, 176/386, and 171/386 respectively. It can be observed that the proposed detector attains the best detection performance in the noise-free cases. Besides, the corner localization accuracy is another important measure to evaluate detectors. It can be observed that for the three test images with ground truths the proposed detector attains the smallest localization error for image 'Lab' and image 'Pentagon' and attains the third smallest localization error for image 'Block', while the CPDA [34], ADCC [42], He & Yung [31], and GCM [36] detectors are moderate, and the ANDD [5], MSCP [29], and ARCSS [35] detectors are the poorest in corner localization.

The second experiment is used to compare the noise robustness of the eight detectors for two noisy test images. The two test images ('Block' and 'Lab') are added with zero-mean Gaussian white noise with variance ε_ω^2 ($\varepsilon_\omega = 1, 2, \ldots, 20$). For each noise variance, 300 experiments were carried out to obtain the average number of missed corners, average number of false corners, and average localization errors. In this evaluation criteria, with the increase of the noise variance, the lower the average slope of the curve, the better the noise robustness of a detector. The three measures for the two images are given in Fig. 11(a)-(c) and (d)-(f) respectively. For the eight detectors (MSCP [29], He & Yung [31], CPDA [34], ARCSS [35], GCM [36], ANDD [5], ADCC [42], and the proposed detector), the three measures gradually become worse with the increase of the noise level. Taking the three measures into account, the proposed method achieves the best results for the noisy test images, and the method has the lowest curve average slope change. The reason is that the proposed method has a
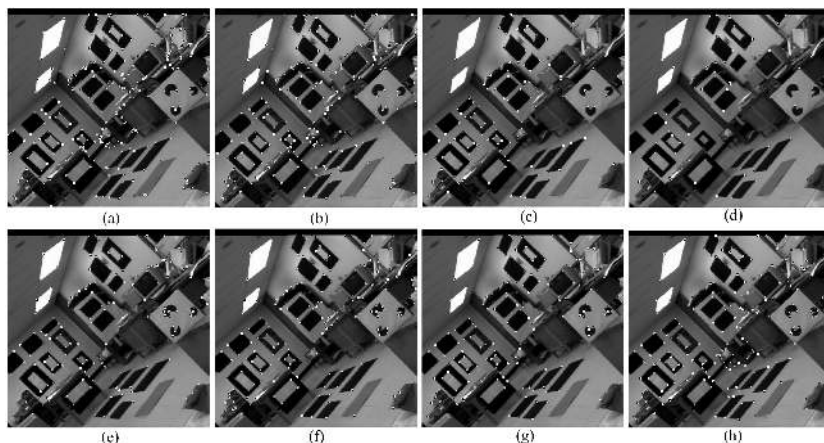
Fig. 9 Detection results on the test image 'Lab'. (a) MSCP detector [29], (b) He & Yung detector [31], (c) CPDA detector [34], (d) ARCSS detector [35], (e) GCM detector [36], (f) ANDD detector [5], (g) ADCC detector [42], and (h) Proposed detector.

TABLE I Performance comparison of the eight detectors for noise-free test images (the unit is in pixel).

Detector	Missed corners			False corners			Localization error		
	Test image 'Block'	Test image 'Lab'	Test image 'Pentagon'	Test image 'Block'	Test image 'Lab'	Test image 'Pentagon'	Test image 'Block'	Test image 'Lab'	Test image 'Pentagon'
MSCP	2	45	4	6	88	92	1.379	1.437	1.571
He & Yung	11	45	9	5	77	72	1.024	1.389	1.483
CPDA	27	122	43	0	12	3	0.952	1.313	1.225
ARCSS	36	180	44	0	7	9	1.302	1.429	1.942
GCM	7	95	32	1	32	7	1.209	1.324	1.253
ANDD	4	94	18	1	50	99	1.326	1.455	2.254
ADCC	5	94	6	1	33	37	1.116	1.295	1.523
Proposed	5	75	19	2	48	22	1.111	1.288	1.219

better capability on noise robustness and corner resolution. The GCM, ADCC, and ANDD detectors are moderate. The He & Yung, MSCP, and ARCSS detectors perform poorly because they are more sensitive to local variation and noise on curves.
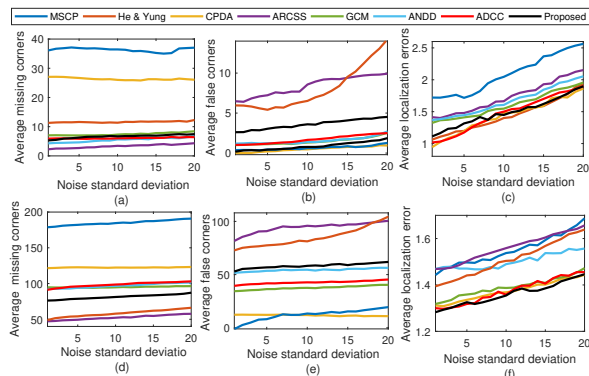

Fig. 11 Demonstration of the noise-robustness of the eight detectors for the test images 'Block' and 'Lab': (a-c) for noisy 'Block' images, and (d-f) for noisy 'Lab' images.

However, there exist some exceptions for the CPDA detector [34]. From Fig. 11(a) and (e), it can be found that the measures for the CPDA detector become better with the increase of noise level. The reason is that the authors of the CPDA detector [34] raise the threshold only to detect 'strong' corners with large curvatures and neglect some obvious corners, as shown in Fig. 8(d) and Fig. 9(d). However, the low corner resolution

makes the CPDA detector uncertain for some corner detection under the influence of different noise levels. Take the sixth corner in Fig. 5(c) as an example, the CPDA detector cannot detect it in the noise-free case as shown in Fig. 8(d), while it can be detected in the noisy case with a standard variance $\varepsilon_\omega = 20$ as shown in Fig. 12(a). The output of the proposed detector is shown in Fig. 12(b) with the same noise level. Compared with the noise-free case, as shown in Fig. 8(h), the change of the result is not obvious. The reason is that the issue of corner resolution and noise robustness without the loss of corner detection accuracy has been considered in our corner measure.
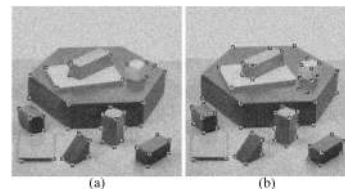

Fig. 12 The effect of corner resolution on corner detectors, (a) CPDA detector [34], (b) Proposed detector.

B. Evaluation of detection performance based on average repeatability

In this section, another performance evaluation for corner detection based on average repeatability [34] is adopted, which has no human involvement and can be used with any size of

database. We had a total of 24 different gray-scale images: one is the 'Block' image [5] and the other 23 images are collected from standard databases [51], [52], which include many commonly used images such as 'Lena', 'Leaf', 'House', and 'Lab'.

We had a total of 8,904 transformed test images, which were obtained by applying the following six different transformations on each original image:

• Rotations: The original image was rotated at 18 different angles within $[-\pi/2, \pi/2]$.

• Uniform scaling: The original image was scaled with scale factors $s_x = s_y$ in $[0.5, 2]$ with 0.1 apart, excluding 1.

• Non-uniform scaling: The scales s_x and s_y were chosen by sampling the ranges $[0.7, 1.5]$ and $[0.5, 1.8]$ with a 0.1 interval respectively.

• Shear transformations: The shear factor c was chosen by sampling the range $[-1, 1]$ with a 0.1 interval, excluding 0, with the following formula

$$\left[\begin{array}{c} x' \\ y' \end{array}\right] = \left[\begin{array}{cc} 1 & c \\ 0 & 1 \end{array}\right] \left[\begin{array}{c} x \\ y \end{array}\right].$$

• Lossy JPEG compression: A JPEG quality factor was chosen by sampling the range $[5, 100]$ with an interval 5.

• Gaussian noise: Zero mean white Gaussian noise was added to the original image at 15 standard deviations in $[1, 15]$ with an interval 1.

In order to have a fair performance comparison in this experiment, for each input image, the average number of detected corners of the eight detectors is marked as the reference corner number for the input image. Then the threshold for each detector is adjusted so that each detector extracts about the same number of corners from each input image. Fig. 13 shows the average repeatability of the eight detectors under rotation, uniform scaling, non-uniform scaling, shear transformation, lossy JPEG compression, and Gaussian noises. Our proposed detector attains the best average repeatability under rotation, uniform scaling, non-uniform scaling, lossy JPEG compression, and Gaussian noises, and achieves the second-best performance with shear transformation. The reason is that the proposed detector has a better capability on corner resolution, detection accuracy, and noise robustness in the discrete domain. The CPDA detector [34] has the best average repeatability under the shear transformation, the second-best performance under uniform scaling, non-uniform scaling, lossy JPEG compression, and Gaussian noises, and the third-best performance for rotation changes. The performances of the GCM [36], ADCC [42], He & Yung [31], ANDD [5], MSCP [29], and ARCSS [35] detectors are moderate. The reason is that the corner detection accuracy, corner resolution, and noise robustness are not considered simultaneously by the seven detectors. The average repeatability and localization error are summarized in Table II. Meanwhile, it can be also found that the performance comparison results on CPDA [34], GCM [36], MSCP [29], He & Yung [31], and ARCSS [35] detectors in this paper are consistent with the performance comparison results given in [53].
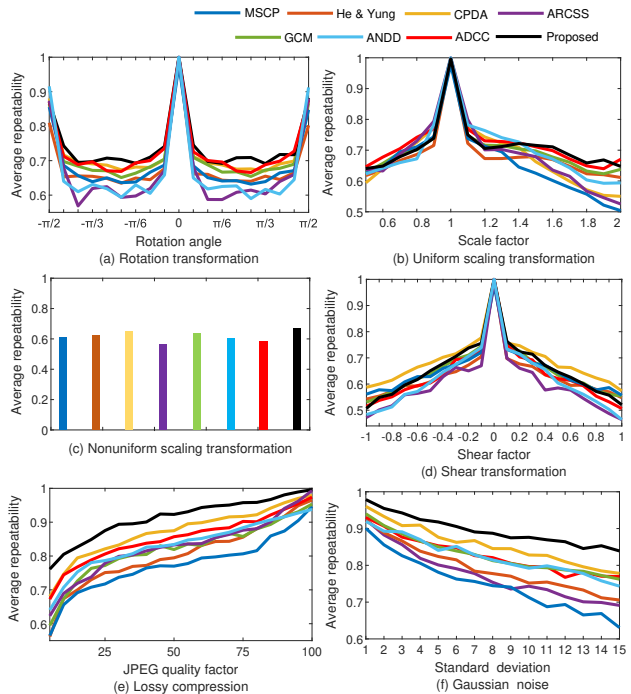

Fig. 13 Average repeatability of the eight detectors under rotation, uniform scaling, non-uniform scaling, shear transforms, lossy JPEG compression, and additive white Gaussian noises.

TABLE II Average repeatability and localization error.

Detector	Repeatability (percentage)	Localization error (pixels)
MSCP	0.612	1.974
He & Yung	0.645	1.818
CPDA	0.711	1.577
ARCSS	0.603	2.064
GCM	0.677	1.635
ANDD	0.622	1.719
ADCC	0.671	1.731
Proposed	0.722	1.518

Based on the aspects of missed and false corners and the localization accuracy for the two commonly used test images which have ground truths with noise-free and different noise levels, the average repeatability under affine transformation, lossy JPEG compression, and noise robustness, the eight detectors have different performances. Fully comparing the performances of the detectors over these four aspects, the proposed detector is the best in overall performance. This is owing to the fact that the proposed detector is less sensitive to local variation and noise on curves while maintaining a high corner resolution, detection capability, and localization accuracy.

C. Average running time

The proposed corner detector has been implemented in MATLAB (R2016a) using a 2.81 GHz CPU with 16 GB of memory. For each test image, the proposed algorithm was executed 100 times and the mean execution time was

measured. The average running time of the eight corner detectors is summarized in Table III. According to Table III, the 'Block' and 'House' images required similar times; the 'Lab', 'Lena', and 'Parking meter' images required more times. Note that the time varies slightly depending on the number of detected edge pixels in the image. Meanwhile, it can be easily concluded that the proposed method meets the requirement of real-time applications.

TABLE III Average running time
(the unit is in second, image size is in pixels).

| Methods | Time (s) | | | | |
| | Block | House | Lab | Lena | Parking meter |
	(256×256)	(256×256)	(512×512)	(512×512)	(558×495)
MSCP	0.058	0.055	0.173	0.246	0.255
He & Yung	0.062	0.059	0.183	0.253	0.261
CPDA	0.143	0.124	0.359	0.347	0.363
ARCSS	0.162	0.159	0.383	0.367	0.392
GCM	0.167	0.144	0.381	0.392	0.402
ANDD	0.984	0.941	4.231	4.491	4.682
ADCC	0.136	0.135	0.318	0.356	0.389
Proposed	0.127	0.106	0.285	0.326	0.290

VI. CONCLUSION

The main contribution of the paper is the development of the discrete curvature representations. The discrete curvature behavior on three corner models is investigated and a number of model properties are specified. A new corner measure is proposed which has high corner resolution and strong ability for noise robust corner detection. Consequently, the corner resolution constant is derived and as a result, a noise robust corner detector is presented. The experimental results show that the proposed detector outperforms the seven state-of-the-art corner detectors in terms of missed corners, false corners, and localization accuracy under different levels of noises, and in average repeatability under affine transformation, lossy JPEG compression, and noise robustness.

APPENDIX A
SOLVING INEQUALITY (17)

It is worth to note that when judging which is larger between two numbers $F(u)$ and $H(u)$, given $F(u) > f(u)$ and $h(u) > H(u)$, if $f(u) > h(u)$, then $F(u) > H(u)$ is established.

For inequality (17), the left-hand side of the inequality is $|\kappa_d(u)_{|u=0}|$ of Equation (11), the right-hand side of inequality is $|\kappa_d(u)_{|u=w/2}|$ of Equation (11). In terms of Equation (11),

$$|\kappa_d(u)_{|u=0}| = \frac{4(2d-w)\cos(\frac{\alpha+\beta}{2})\cos(\frac{\pi}{4}-\frac{\alpha}{2})\cos(\frac{\pi}{4}-\frac{\beta}{2}) + 2w\cos\alpha}{d^2(1+\sin\alpha)^{3/2}}$$
$$> \frac{2w\cos\alpha}{d^2(1+\sin\alpha)^{3/2}}, \quad (44)$$

and

$$|\kappa_d(u)_{|u=w/2}| = \frac{2(2d-w/2)\cos(\frac{\alpha+\beta}{2})\left((2d-w)\sin(\frac{\alpha+\beta}{2}) + w\cos(\frac{\alpha-\beta}{2})\right)}{\left(\left((2d-w)\sin(\frac{\alpha+\beta}{2}) + w\cos(\frac{\alpha-\beta}{2})\right)^2 + w^2\sin^2(\frac{\alpha-\beta}{2})\right)^{3/2}}$$
(45)

It is easy to prove that

$$|\kappa_d(u)_{|u=w/2}| \leq \frac{\frac{\sqrt{2}}{2}(2d-w/2)\cos(\frac{\alpha+\beta}{2})}{w^{3/2}\left((2d-w)\sin(\frac{\alpha+\beta}{2}) + w\cos(\frac{\alpha-\beta}{2})\right)^{1/2}|\sin^{3/2}(\frac{\alpha-\beta}{2})|}$$
(46)

Inequality (46) can be rewritten as

$$|\kappa_d(u)_{|u=w/2}| \leq \frac{(2d-w/2)\cos(\frac{\alpha+\beta}{2})}{2w^2\left(\frac{\cos(\frac{\alpha-\beta}{2})+\sin(\frac{\alpha+\beta}{2})}{2\cos(\frac{\alpha-\beta}{2})+\sin(\frac{\alpha+\beta}{2})}\cos(\frac{\alpha-\beta}{2})\right)^{1/2}|\sin^{3/2}(\frac{\alpha-\beta}{2})|}$$
(47)

Then, inequality (17) is established when it satisfies

$$\frac{2w\cos\alpha}{d^2(1+\sin\alpha)^{3/2}} \geq \frac{(2d-w/2)\cos(\frac{\alpha+\beta}{2})}{2w^2\left(\frac{\cos(\frac{\alpha-\beta}{2})+\sin(\frac{\alpha+\beta}{2})}{2\cos(\frac{\alpha-\beta}{2})+\sin(\frac{\alpha+\beta}{2})}\cos(\frac{\alpha-\beta}{2})\right)^{1/2}|\sin^{3/2}(\frac{\alpha-\beta}{2})|}.$$
(48)

In this case, $d \in [w/2, w)$, then inequality (48) can be further written as inequality (18).

APPENDIX B
SOLVING INEQUALITY (19)

For (19), denote

$$\Omega = 2d^2(1 - \cos(\alpha+\beta)) + 2w^2(1 - \sin\beta) + 2dw(\sin\alpha + \sin\beta + \cos(\alpha+\beta) - 1).$$
(49)

For (49), it can be concluded
With $\frac{\alpha+\beta}{2} \in \left(-\frac{\pi}{2}, 0\right)$,

$$\Omega \leq 4d^2\sin^2(\frac{\alpha+\beta}{2}) + 4w^2\sin^2(\frac{\pi}{4} - \frac{\beta}{2}).$$
(50)

With $\frac{\alpha+\beta}{2} \in \left[0, \frac{\pi}{2}\right)$,

$$\Omega \leq \left(2d\sin(\frac{\alpha+\beta}{2}) + 2w\sin(\frac{\pi}{4} - \frac{\beta}{2})\right)^2.$$
(51)

For (19), it can be found that

$$(4d - 3w)\sin(\alpha+\beta) + 3w\cos\alpha + w\cos\beta = 0 \quad (52)$$

holds when

$$\frac{\alpha+\beta}{2} = \arcsin\left(-\frac{w(3\cos\alpha + \cos\beta)}{2(4d-3w)\cos(\frac{\alpha+\beta}{2})}\right).$$
(53)

In terms of (46), (49)-(53), inequality (19) with $d \in [w, \tau w]$ is established when it satisfies

a) With $\frac{\alpha+\beta}{2} \in \left(-\frac{\pi}{2}, \arcsin\left(-\frac{w(3\cos\alpha+\cos\beta)}{2(4d-3w)(\cos(\frac{\alpha+\beta}{2}))}\right)\right)$,

$$-\frac{d((4d-3w)\sin(\alpha+\beta)+3w\cos\alpha+w\cos\beta)}{\left(4d^2\sin^2(\frac{\alpha+\beta}{2})+4w^2\sin^2(\frac{\pi}{4}-\frac{\beta}{2})\right)^{3/2}} >$$
$$\frac{\frac{\sqrt{2}}{2}(2d-w/2)\cos(\frac{\alpha+\beta}{2})}{w^{3/2}|(2d-w)\sin(\frac{\alpha+\beta}{2})+w\cos(\frac{\alpha-\beta}{2})|^{1/2}|\sin^{3/2}(\frac{\alpha-\beta}{2})|}. \tag{54}$$

Inequality (54) can be further written as inequality (20).

b) With $\frac{\alpha+\beta}{2} \in \left(\arcsin\left(-\frac{w(3\cos\alpha+\cos\beta)}{2(4d-3w)(\cos(\frac{\alpha+\beta}{2}))}\right), 0\right)$,

$$\frac{d((4d-3w)\sin(\alpha+\beta)+3w\cos\alpha+w\cos\beta)}{\left(4d^2\sin^2(\frac{\alpha+\beta}{2})+4w^2\sin^2(\frac{\pi}{4}-\frac{\beta}{2})\right)^{3/2}} >$$
$$\frac{\frac{\sqrt{2}}{2}(2d-w/2)\cos(\frac{\alpha+\beta}{2})}{w^{3/2}|(2d-w)\sin(\frac{\alpha+\beta}{2})+w\cos(\frac{\alpha-\beta}{2})|^{1/2}|\sin^{3/2}(\frac{\alpha-\beta}{2})|}. \tag{55}$$

Inequality (55) can be further written as inequality (21).

c) With $\frac{\alpha+\beta}{2} \in \left[0, \frac{\pi}{2}\right)$,

$$\frac{d((4d-3w)\sin(\alpha+\beta)+3w\cos\alpha+w\cos\beta)}{\left(2d\sin(\frac{\alpha+\beta}{2})+2w\sin(\frac{\pi}{4}-\frac{\beta}{2})\right)^3} >$$
$$\frac{\frac{\sqrt{2}}{2}(2d-w/2)\cos(\frac{\alpha+\beta}{2})}{w^{3/2}\left((2d-w)\sin(\frac{\alpha+\beta}{2})+w\cos(\frac{\alpha-\beta}{2})\right)^{1/2}|\sin^{3/2}(\frac{\alpha-\beta}{2})|}. \tag{56}$$

Inequality (56) can be further written as inequality (22).

Appendix C
Solving inequality (26)

For (26), $d \in [w/2, w)$, the right-hand side of inequality (26) is

$$|\kappa_d(u)_{|u=w/2}| =$$
$$\frac{2(2d-w/2)\left|\sin(\frac{\beta-\alpha}{2})\left((2d-w)\cos(\frac{\beta-\alpha}{2})+w\sin(\frac{\alpha+\beta}{2})\right)\right|}{\left(\left((2d-w)\cos(\frac{\beta-\alpha}{2})+w\sin(\frac{\alpha+\beta}{2})\right)^2+w^2\cos^2(\frac{\alpha+\beta}{2})\right)^{3/2}}$$
$$\leq \frac{2(2d-w/2)|\sin(\frac{\beta-\alpha}{2})|}{\left(2d\cos(\frac{\beta-\alpha}{2})-2w\sin(\frac{\pi}{4}-\frac{\beta}{2})\sin(\frac{\pi}{4}-\frac{\alpha}{2})\right)^2} \tag{57}$$

For (26), denote

$$\Psi = (2d-w)(\cos\alpha-\cos\beta+\sin(\beta-\alpha))+2w\cos\alpha$$
$$= 8d\sin(\frac{\beta-\alpha}{2})\cos(\frac{\pi}{4}-\frac{\alpha}{2})\cos(\frac{\pi}{4}-\frac{\beta}{2})+ \tag{58}$$
$$4w\cos(\frac{\alpha-\beta}{2})\cos(\frac{\pi}{4}-\frac{\alpha}{2})\sin(\frac{\pi}{4}-\frac{\beta}{2}).$$

For (58), it can be found that $\Psi = 0$ holds when

$$\frac{\beta-\alpha}{2} = \arctan\left(-\frac{w}{2d}\tan\left(\frac{\pi}{4}-\frac{\beta}{2}\right)\right). \tag{59}$$

Meanwhile, the left-hand side of inequality (26) can be written as

$$|\kappa_d(u)_{|u=0}|$$
$$= \frac{|2d\sin(\frac{\beta-\alpha}{2})\cos(\frac{\pi}{4}-\frac{\beta}{2})+w\cos(\frac{\beta-\alpha}{2})\sin(\frac{\pi}{4}-\frac{\beta}{2})|}{2d^2\cos^2(\frac{\pi}{4}-\frac{\alpha}{2})}. \tag{60}$$

Then, solving inequality (26) as follows

a) With $\frac{\beta-\alpha}{2} \in \left(-\frac{\pi}{2}, \arctan\left(-\frac{w}{2d}\tan(\frac{\pi}{4}-\frac{\beta}{2})\right)\right)$, Equation (60) can be reduced to

$$|\kappa_d(u)_{|u=0}|$$
$$\geq \frac{|\sin(\frac{\beta-\alpha}{2})|\cos(\frac{\pi}{4}-\frac{\beta}{2})-\cos(\frac{\beta-\alpha}{2})\sin(\frac{\pi}{4}-\frac{\beta}{2})}{d\cos^2(\frac{\pi}{4}-\frac{\alpha}{2})} \tag{61}$$

In this case, inequality (26) is established when it satisfies

$$\frac{|\sin(\frac{\beta-\alpha}{2})|\cos(\frac{\pi}{4}-\frac{\beta}{2})-\cos(\frac{\beta-\alpha}{2})\sin(\frac{\pi}{4}-\frac{\beta}{2})}{d\cos^2(\frac{\pi}{4}-\frac{\alpha}{2})} \geq$$
$$\frac{2(2d-w/2)|\sin(\frac{\beta-\alpha}{2})|}{\left(2d\cos(\frac{\beta-\alpha}{2})-2w\sin(\frac{\pi}{4}-\frac{\beta}{2})\sin(\frac{\pi}{4}-\frac{\alpha}{2})\right)^2}. \tag{62}$$

Inequality (62) can be further written as inequality (27).

b) With $\frac{\beta-\alpha}{2} \in \left(\arctan\left(-\frac{w}{2d}\tan(\frac{\pi}{4}-\frac{\beta}{2})\right), \frac{\pi}{2}\right)$, Equation (60) becomes

$$|\kappa_d(u)_{|u=0}|$$
$$\geq \frac{2\sin(\frac{\beta-\alpha}{2})\cos(\frac{\pi}{4}-\frac{\beta}{2})+\cos(\frac{\beta-\alpha}{2})\sin(\frac{\pi}{4}-\frac{\beta}{2})}{2d\cos^2(\frac{\pi}{4}-\frac{\alpha}{2})} \tag{63}$$

In this case, inequality (26) is established when it satisfies

$$\frac{2\sin(\frac{\beta-\alpha}{2})\cos(\frac{\pi}{4}-\frac{\beta}{2})+\cos(\frac{\beta-\alpha}{2})\sin(\frac{\pi}{4}-\frac{\beta}{2})}{2d\cos^2(\frac{\pi}{4}-\frac{\alpha}{2})} \geq$$
$$\frac{2(2d-\frac{w}{2})|\sin(\frac{\beta-\alpha}{2})|}{\left(2d\cos(\frac{\beta-\alpha}{2})-2w\sin(\frac{\pi}{4}-\frac{\beta}{2})\sin(\frac{\pi}{4}-\frac{\alpha}{2})\right)^2}. \tag{64}$$

Inequality (64) can be further written as inequality (29).

Appendix D
Solving inequality (31)

For (31), denote

$$\Lambda = 3w\cos\alpha+(4d-3w)\sin(\beta-\alpha)-w\cos\beta. \tag{65}$$

For (65), it can be found that $\Lambda = 0$ holds when

$$\frac{\beta-\alpha}{2} =$$
$$\arcsin\left(\frac{-w\cos\alpha}{4(d-w)\cos(\frac{\beta-\alpha}{2})+2w\cos(\frac{\pi}{4}-\frac{\alpha}{2})\cos(\frac{\pi}{4}-\frac{\beta}{2})}\right). \tag{66}$$

For (31), denote

$$\Theta = 2d^2(1+\cos(\beta-\alpha))+2w^2(1-\sin\beta)+$$
$$2dw(\sin\alpha+\sin\beta-\cos(\beta-\alpha)-1) \tag{67}$$
$$\leq 4d^2\cos^2(\frac{\beta-\alpha}{2})+4w^2\cos^2(\frac{\pi}{4}+\frac{\beta}{2})$$

Meanwhile, the right-hand side of inequality (31) can be written as

$$|\kappa_d(u)_{|u=w/2}| \leq \frac{2(2d-w/2)\left|\sin(\frac{\beta-\alpha}{2})\right|}{\left((2d-w)\cos(\frac{\beta-\alpha}{2}) + w\sin(\frac{\alpha+\beta}{2})\right)^2} \quad (68)$$

Then inequality (31) is established when it satisfies

a) With $\frac{\beta-\alpha}{2} \in$
$$\left(-\frac{\pi}{2}, \arcsin\left(\frac{-w\cos\alpha}{4(d-w)\cos(\frac{\beta-\alpha}{2})+2w\cos(\frac{\pi}{4}-\frac{\alpha}{2})\cos(\frac{\pi}{4}-\frac{\beta}{2})}\right)\right),$$

$$-\frac{d\left((4d-3w)\sin(\beta-\alpha)+3w\cos\alpha-w\cos\beta\right)}{\left(4d^2\cos^2(\frac{\beta-\alpha}{2})+4w^2\cos^2(\frac{\pi}{4}+\frac{\beta}{2})\right)^{3/2}}$$
$$> \frac{2(2d-w/2)\left|\sin(\frac{\beta-\alpha}{2})\right|}{\left((2d-w)\cos(\frac{\beta-\alpha}{2})+w\sin(\frac{\alpha+\beta}{2})\right)^2} \quad (69)$$

Inequality (69) can be further written as inequality (32).

b) With $\frac{\beta-\alpha}{2} \in$
$$\left(\arcsin\left(\frac{-w\cos\alpha}{4(d-w)\cos(\frac{\beta-\alpha}{2})+2w\cos(\frac{\pi}{4}-\frac{\alpha}{2})\cos(\frac{\pi}{4}-\frac{\beta}{2})}\right), \frac{\pi}{2}\right),$$

$$\frac{d\left((4d-3w)\sin(\beta-\alpha)+3w\cos\alpha-w\cos\beta\right)}{\left(4d^2\cos^2(\frac{\beta-\alpha}{2})+4w^2\cos^2(\frac{\pi}{4}+\frac{\beta}{2})\right)^{3/2}}$$
$$> \frac{2(2d-w/2)\left|\sin(\frac{\beta-\alpha}{2})\right|}{\left((2d-w)\cos(\frac{\beta-\alpha}{2})+w\sin(\frac{\alpha+\beta}{2})\right)^2} \quad (70)$$

Inequality (70) can be further written as inequality (33).

Acknowledgment

Reference

[1] Y. Pang, J. Cao, X. Li, Learning sampling distributions for efficient object detection, IEEE Transactions on Cybernetics 47 (1) (2017) 117–129.

[2] Z. Shao, Y. Li, On integral invariants for effective 3-D motion trajectory matching and recognition, IEEE Transactions on Cybernetics 46 (2) (2016) 511–523.

[3] H. P. Moravec, Visual mapping by a robot rover, in: Proceedings of the 6th International Joint Conference on Artificial Intelligence-Vol. 1, Morgan Kaufmann Publishers Inc., 1979, pp. 598–600.

[4] C.-H. Teh, R. T. Chin, On the detection of dominant points on digital curves, IEEE Transactions on Pattern Analysis and Machine Intelligence 11 (8) (1989) 859–872.

[5] P.-L. Shui, W.-C. Zhang, Corner detection and classification using anisotropic directional derivative representations, IEEE Transactions on Image Processing 22 (8) (2013) 3204–3218.

[6] C. Harris, M. Stephens, A combined corner and edge detector, in: Alvey Vision Conference, 1988, pp. 147–151.

[7] J. A. Noble, Finding corners, Image and Vision Computing 6 (2) (1988) 121–128.

[8] T. Kadir, M. Brady, Saliency, scale and image description, International Journal of Computer Vision 45 (2) (2001) 83–105.

[9] T. Lindeberg, Junction detection with automatic selection of detection scales and localization scales, in: IEEE International Conference on Image Processing, Vol. 1, 1994, pp. 924–928.

[10] C. Schmid, R. Mohr, C. Bauckhage, Evaluation of interest point detectors, International Journal of Computer Vision 37 (2) (2000) 151–172.

[11] D. G. Lowe, Distinctive image features from scale-invariant keypoints, International Journal of Computer Vision 60 (2) (2004) 91–110.

[12] K. Mikolajczyk, C. Schmid, Scale & affine invariant interest point detectors, International Journal of Computer Vision 60 (1) (2004) 63–86.

[13] H. Bay, T. Tuytelaars, L. Van Gool, SURF: Speeded up robust features, Computer Vision–ECCV (2006) 404–417.

[14] D. Marimon, A. Bonnin, T. Adamek, R. Gimeno, DARTs: Efficient scale-space extraction of DAISY keypoints, in: IEEE Conference on Computer Vision and Pattern Recognition (CVPR), 2010, pp. 2416–2423.

[15] W. A. Albukhanajer, J. A. Briffa, Y. Jin, Evolutionary multiobjective image feature extraction in the presence of noise, IEEE Transactions on Cybernetics 45 (9) (2015) 1757–1768.

[16] H. Li, Y. Wei, L. Li, C. P. Chen, Hierarchical feature extraction with local neural response for image recognition, IEEE Transactions on Cybernetics 43 (2) (2013) 412–424.

[17] R. Deriche, G. Giraudon, A computational approach for corner and vertex detection, International Journal of Computer Vision 10 (2) (1993) 101–124.

[18] S. M. Smith, J. M. Brady, Susan-a new approach to low level image processing, International Journal of Computer Vision 23 (1) (1997) 45–78.

[19] L. Parida, D. Geiger, R. Hummel, Junctions: Detection, classification, and reconstruction, IEEE Transactions on Pattern Analysis and Machine Intelligence 20 (7) (1998) 687–698.

[20] M. A. Ruzon, C. Tomasi, Edge, junction, and corner detection using color distributions, IEEE Transactions on Pattern Analysis and Machine Intelligence 23 (11) (2001) 1281–1295.

[21] E. D. Sinzinger, A model-based approach to junction detection using radial energy, Pattern Recognition 41 (2) (2008) 494–505.

[22] E. Rosten, R. Porter, T. Drummond, Faster and better: A machine learning approach to corner detection, IEEE Transactions on Pattern Analysis and Machine Intelligence 32 (1) (2010) 105–119.

[23] R. Elias, R. Laganière, Judoca: Junction detection operator based on circumferential anchors, IEEE Transactions on Image Processing 21 (4) (2012) 2109.

[24] G.-S. Xia, J. Delon, Y. Gousseau, Accurate junction detection and characterization in natural images, International Journal of Computer Vision 106 (1) (2014) 31–56.

[25] T.-A. Pham, M. Delalandre, S. Barrat, J.-Y. Ramel, Accurate junction detection and characterization in line-drawing images, Pattern Recognition 47 (1) (2014) 282–295.

[26] A. Rattarangsi, R. T. Chin, Scale-based detection of corners of planar curves, in: 10th International Conference on Pattern Recognition, Vol. 1, 1990, pp. 923–930.

[27] D.-M. Tsai, M.-F. Chen, Curve fitting approach for tangent angle and curvature measurements, Pattern Recognition 27 (5) (1994) 699–711.

[28] F. Mokhtarian, R. Suomela, Robust image corner detection through curvature scale space, IEEE Transactions on Pattern Analysis and Machine Intelligence 20 (12) (1998) 1376–1381.

[29] X. Zhang, M. Lei, D. Yang, Y. Wang, L. Ma, Multi-scale curvature product for robust image corner detection in curvature scale space, Pattern Recognition Letters 28 (5) (2007) 545–554.

[30] B. Zhong, W. Liao, Direct curvature scale space: Theory and corner detection, IEEE Transactions on Pattern Analysis and Machine Intelligence 29 (3) (2007) 100–108.

[31] X. C. He, N. H. Yung, Corner detector based on global and local curvature properties, Optical Engineering 47 (5) (2008) 057008–057008.

[32] C. F. Olson, Adaptive-scale filtering and feature detection using range data, IEEE Transactions on Pattern Analysis and Machine Intelligence 22 (9) (2000) 983–991.

[33] F. Mokhtarian, N. Khalili, P. Yuen, Multi-scale free-form 3D object recognition using 3D models, Image and Vision Computing 19 (5) (2001) 271–281.

[34] M. Awrangjeb, G. Lu, Robust image corner detection based on the chord-to-point distance accumulation technique, IEEE Transactions on Multimedia 10 (6) (2008) 1059–1072.

[35] M. Awrangjeb, G. Lu, An improved curvature scale-space corner detector and a robust corner matching approach for transformed image identification, IEEE Transactions on Image Processing 17 (12) (2008) 2425–2441.

[36] X. Zhang, H. Wang, A. W. Smith, X. Ling, B. C. Lovell, D. Yang, Corner detection based on gradient correlation matrices of planar curves, Pattern Recognition 43 (4) (2010) 1207–1223.

[37] W.-C. Zhang, F.-P. Wang, L. Zhu, Z.-F. Zhou, Corner detection using Gabor filters, IET Image Processing 8 (11) (2014) 639–646.

[38] W.-C. Zhang, P.-L. Shui, Contour-based corner detection via angle difference of principal directions of anisotropic Gaussian directional derivatives, Pattern Recognition 48 (9) (2015) 2785–2797.

[39] S. W. Teng, R. M. N. Sadat, G. Lu, Effective and efficient contour-based corner detectors, Pattern Recognition 48 (7) (2015) 2185–2197.

[40] X. Zhang, Y. Qu, D. Yang, H. Wang, J. Kymer, Laplacian scale-space behavior of planar curve corners, IEEE Transactions on Pattern Analysis and Machine Intelligence 37 (11) (2015) 2207–2217.

[41] A. M. Pinheiro, M. Ghanbari, Piecewise approximation of contours through scale-space selection of dominant points, IEEE Transactions on Image Processing 19 (6) (2010) 1442–1450.

[42] S. Chen, H. Meng, C. Zhang, C. Liu, A KD curvature based corner detector, Neurocomputing 173 (2016) 434–441.

[43] P.-L. Shui, W.-C. Zhang, Noise-robust edge detector combining isotropic and anisotropic Gaussian kernels, Pattern Recognition 45 (2) (2012) 806–820.

[44] A. Desolneux, L. Moisan, J.-M. Morel, Meaningful alignments, International Journal of Computer Vision 40 (1) (2000) 7–23.

[45] V. Borrelli, F. Orgeret, Error term in pointwise approximation of the curvature of a curve, Computer Aided Geometric Design 27 (7) (2010) 538–550.

[46] A. Witkin, Scale-space filtering: A new approach to multi-scale description, in: IEEE International Conference on Acoustics, Speech, and Signal Processing, Vol. 9, 1984, pp. 150–153.

[47] M. Trajković, M. Hedley, Fast corner detection, Image and Vision Computing 16 (2) (1998) 75–87.

[48] M. Worring, A. W. M. Smeulders, Digital curvature estimation, CVGIP: Image Understanding 58 (3) (1993) 366–382.

[49] S. Hermann, R. Klette, A Comparative Study on 2D Curvature Estimators, in: International Conference on Computing: Theory & Applications, 2006.

[50] J. Canny, A computational approach to edge detection, IEEE Transactions on Pattern Analysis and Machine Intelligence (6) (1986) 679–698.

[51] http://www.petitcolas.net/fabien/watermarking/image_database/index.html/.

[52] http://sipi.usc.edu/database/.

[53] M. Awrangjeb, G. Lu, C. S. Fraser, Performance comparisons of contour-based corner detectors, IEEE Transactions on Image Processing 21 (9) (2012) 4167–4179.

Toby Breckon is currently a Reader (UK Associate Professor) within the School of Engineering and Computer Sciences, Durham University (UK). His key research interests lie in the domain of computer vision and image processing and he leads a range of research activity in this area. Dr. Breckon holds a PhD in informatics (computer vision) from the University of Edinburgh (UK). Dr. Breckon is a Chartered Engineer, Chartered Scientist and a Fellow of the British Computer Society.

Naif Alshammari is a lecturer at Majmaah University (KSA). He is currently a PhD student at the School of Engineering and Computer Science, Durham University (UK). His research interests include object detection and segmentation using state of the art technique Convolutional Neural Networks (CNNs). He is working on the challenging topics of automotive scene understanding under extreme variations in environmental conditions such as varying illumination and adverse weather.

Weichuan Zhang received the MS degree in signal and information processing from Southwest Jiaotong University in China and the PhD degree in signal and information processing in National Lab of Radar Signal Processing, Xidian University, China. He is a lecturer at Xi'an Polytechnic University. He currently is an academic visitor at CSIRO, Sydney, Australia. His research interests include computer vision, image analysis, and pattern recognition.

Changming Sun received his PhD degree in computer vision from Imperial College London, London, UK in 1992. He then joined CSIRO, Sydney, Australia, where he is currently a Principal Research Scientist carrying out research and working on applied projects. His current research interests include computer vision, image analysis, and pattern recognition. He has served on the program/organizing committees of various international conferences. He is an Associate Editor of the EURASIP Journal on Image and Video Processing. He is a member of the Australian Pattern Recognition Society.